doi:10.1016/j.jmb.2005.07.002 J. Mol. Biol. (2005) 352, 338–354

JMB

Available online at www.sciencedirect.com

SCIENCE DIRECT®

ELSEVIER

Structure and Dynamics of the Homodimeric Dynein Light Chain km23

Udayar Ilangovan[1]†, Wei Ding[2]†, Yan Zhong[2], Christina L. Wilson[2] Jay C. Groppe[1], James T. Trbovich[1], Jorge Zúñiga[1], Borries Demeler[1] Qian Tang[2], Guofeng Gao[2], Kathleen M. Mulder[2]* and Andrew P. Hinck[1]*

[1]*Department of Biochemistry University of Texas Health Science Center at San Antonio San Antonio, TX 78229, USA*

[2]*Department of Pharmacology Penn State College of Medicine Hershey, PA 17033, USA*

**Corresponding authors*

km23 (96 residues, 11 kDa) is the mammalian ortholog of *Drosophila* roadblock, the founding member of LC7/robl/km23 class of dynein light chains. km23 has been shown to be serine-phosphorylated following TGFβ receptor activation and to bind the dynein intermediate chain in response to such phosphorylation. Here, we report the three-dimensional solution structure of km23, which is shown to be that of a homodimer, similar to that observed for the heterodimeric complex formed between p14 and MP1, two distantly related members of the MglB/robl superfamily, but distinct from the LC8 and Tctex-1 classes of dynein light chains, which also adopt homodimeric structures. The conserved surface residues of km23, including three serine residues, are located predominantly on a single face of the molecule. Adjacent to this face is a large cleft formed by the incomplete overlap of loops from opposite monomers. As shown by NMR relaxation data collected at two fields, several cleft residues are flexible on the ns–ps and ms–μs timescales. Based on these observations, we propose that the patch of conserved residues on the central face of the molecule corresponds to the site at which km23 binds the dynein intermediate chain and that the flexible cleft formed between the overlap of loops from the two monomers corresponds to the site at which km23 binds other partners, such as the TGFβ type II receptor or Smad2.

Keywords: NMR; flexibility; dynein light chains; km23; TGFβ

Introduction

Cytoplasmic dynein is a motor complex that transports membrane vesicles and diverse motor cargoes along microtubules (MTs) in a retrograde manner.[1–4] It plays a pivotal role in mitotic spindle assembly and orientation, positioning of the Golgi apparatus, and transport of intracellular organelles, including endosomes and lysosomes.[5,6] The dynein motor complex consists of two heavy chains (~530 kDa), two intermediate chains (~74 kDa), light-intermediate chains (~50–60 kDa), and several light chains (8–22 kDa).[1–4] Dynein heavy chains contain the MT binding sites and the ATP hydrolysis sites that are essential for force production and the movement of the motor complex along MTs.[7,8] The intermediate chains, light-intermediate chains, and light chains form the base of the dynein complex and are important for cargo binding.[1–4]

Three classes of cytoplasmic dynein light chains (DLCs) have been identified in mammals, including LC8, Tctex-1/rp3, and LC7/robl/km23.[1–4,9,10] In addition to binding the dynein intermediate chain (DIC) at distinct regions,[11] light chains have also been shown to directly interact with a number of proteins to exert diverse functions. LC8, for example, binds to neuronal nitric oxide synthase (nNOS),[12,13] the proapoptotic Bcl-2 family members Bim and Bmf,[14,15] the *Drosophila* mRNA localization protein Swallow,[16] and the rabies virus P protein.[17] LC8 has also been reported to be a physiologically

† U.I. & W.D. contributed equally to this work.

Abbreviations used: DLC, Dynein light chain; DIC, dynein intermediate chain; EV, empty vector; IP, immunoprecipitation; HSQC, heteronuclear single quantum coherence; NOE, nuclear Overhauser effect; NOESY, NOE spectroscopy; CSI, chemical shift index; RDC, residual dipolar coupling.

E-mail addresses of the corresponding authors: kmm15@psu.edu; hinck@uthscsa.edu

interacting substrate of p21-activated kinase 1 (Pak1).[18] Pak1 interacts with the complex of LC8 and Bim, and phosphorylates both proteins.[18] Tctex-1 has been shown to interact with Doc2,[19] $p59^{fyn}$ Src family tyrosine protein kinase,[20] and the C-terminal tail of rhodopsin.[21]

LC8 has been studied using both NMR[22,23] and X-ray crystallography[24] and has been shown to adopt a homodimeric structure stabilized by an extensive array of contacts between edge β-strands. Tctex-1 has also been studied structurally and has been shown to adopt a homodimeric structure similar to that of LC8.[25,26] The mechanism of nNOS and Bim peptide binding by LC8 has been investigated by NMR.[22,27] These studies have shown that despite their disparate sequences, each binds in a similar manner in a flexible groove at the homodimer interface.

LC7 was initially identified as a component of the *Chlamydomonas* outer dynein arm,[9] whereas robl was identified in *Drosophila* in a mutant screen for sluggish motility.[9] km23 (96 residues, 11 kDa) and km23-2, a km23 homolog with 77% sequence identity, are the mammalian orthologs of *Chlamydomonas* LC7 and *Drosophila* robl.[10] km23 was discovered in a novel screen for TGFβ receptor-interacting proteins, and has been shown to function both as a DLC and a TGFβ signaling intermediate.[10,28]

The hormone-like polypeptide growth factor TGFβ is known to be an important negative regulator of cell growth and a potent inducer of extracellular matrix synthesis.[29,30] TGFβ initiates its response by binding and bringing together two pairs of structurally similar, single-pass transmembrane receptors, classified as types I (TβRI) and II (TβRII). The ligand-mediated assembly of these two receptor types triggers an intracellular phosphorylation cascade initiated by the serine-threonine kinase domain of the type II receptor, which *trans*-phosphorylates the adjacent type I kinase. The type I kinase in turn phosphorylates the nuclear-translocating Smad proteins, which together with various transcriptional coactivators and corepressors, regulate transcription of target genes.[29,30]

km23 has also been shown to undergo rapid phosphorylation on serine after TGFβ receptor activation, in keeping with the kinase specificity of TβRI and TβRII.[10] TGFβ has been further shown to induce, in a manner dependent upon the kinase activity of TβRII, recruitment of km23 to the DIC.[10] Overexpression of km23 has been shown to induce specific TGFβ responses, including Jun N-terminal kinase (JNK) activation, c-Jun phosphorylation, and cell growth inhibition,[10] while blockade of km23 expression using small interfering RNA (siRNA) results in a decrease in cellular responses to TGFβ, including induction of fibronectin expression and inhibition of cell cycle progression.[28] Thus, km23 appears to play an important role in TGFβ signaling, which may explain the high frequency (42%) with which km23 is altered in cancerous, but not normal ovarian tissue.[28,31]

LC7/robl/km23 DLCs belong to an ancient superfamily of proteins, known as the MglB/robl superfamily, with representative members in all three kingdoms of life.[9,10,32] Members of the MglB family have been implicated in NTPase regulation in bacteria and archae and in regulating the mitogen-activated protein kinase (MAPK) and other signaling pathways in eukaryotes. Recently, the crystal structure of a heterodimer formed between two members of the MglB family, p14 and the MAPK scaffolding protein, MP1, was reported.[33,34] This revealed that the two chains adopt the same overall fold and that they interact through edge β-strands and through helix–helix contacts using hydrophobic residues conserved throughout the superfamily. The overall fold of the dimer is distinct relative to that of the LC8 and Tctex-1 dimers, which has led to the notion that proteins of the MglB/robl superfamily each adopt similar dimeric structures and that their ability to interact with one another to form dimers contributes to the diversity of their functions.[33]

The results presented here show that km23 also adopts the structure of a homodimer similar to that of the p14/MP1 heterodimer.[33,34] The conserved surface residues of km23, including three serine residues, are located predominantly on a single face of the molecule. There is adjacent to this face a large cleft formed by the incomplete overlap of loops from the two monomers. This region of km23 was demonstrated through analysis of NMR relaxation data at two fields to be flexible on the ms–μs and ns-ps timescales. Based on these observations, we propose that the patch of conserved residues on the central face of the molecule corresponds to the site at which km23 binds DIC and that the flexible cleft formed between the overlap of the two monomers corresponds to the site that accommodates both TβRII and Smads.

Results

km23 forms homo-oligomers and hetero-oligomers *in vivo*

Our initial studies to identify regions of km23 important for DIC binding were carried out by generating ten-residue deletions throughout the length of the protein. These deletions each abrogated DIC binding, indicating that the overall fold of the protein, or possibly its dimerization, might be required for its function. The initial goal, therefore, was to characterize km23 with respect to formation of higher-order structure.

Our *in vivo* characterization of higher-order structure was carried out by performing immunoprecipitation/immunoblotting (IP/blot) analyses in 293T cells transfected with V5-tagged km23 (km23-V5) together with either Flag-tagged km23 (km23-Flag) or empty vector (EV). The results, shown in Figure 1(a), revealed that km23-V5 and km23-Flag were in the same immunocomplex when

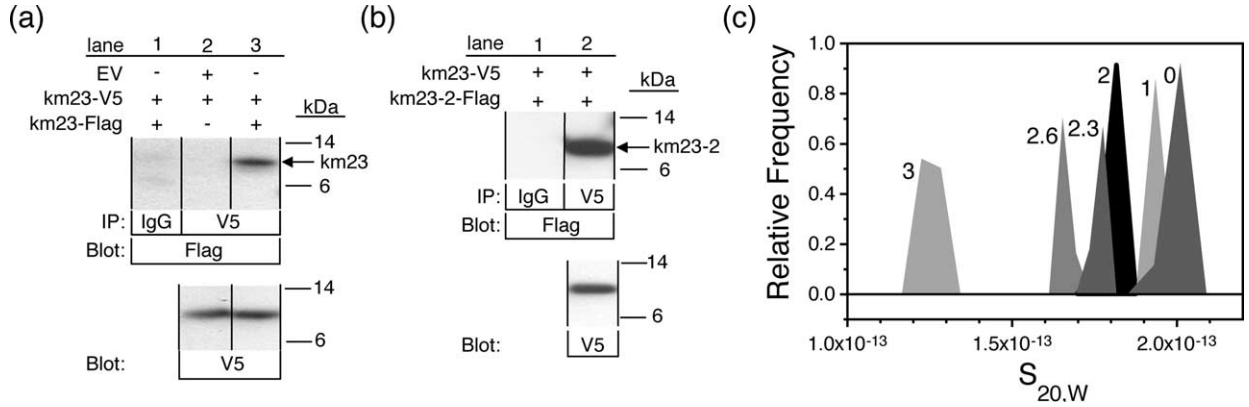

Figure 1. km23 isoforms form homo-oligomers and hetero-oligomers *in vivo* and *in vitro*. (a) km23 forms homo-oligomers as shown through IP-blot analysis of total lysates from 293T cells that had been transfected with V5 and Flag-tagged km23 constructs (top panel, lane 3). Specificity of the immunocomplex is demonstrated by the empty vector (EV) and antibody controls shown in lanes 1 and 2, respectively (top panel). Controls for the expression of km23-V5 were verified by Western blotting whole cell lysates using an anti-V5 antibody (bottom panel, lanes 2 and 3). (b) km23 forms hetero-oligomers with km23-2 as shown through IP-blot analysis of total lysates from 293T cells that had been transfected with V5-tagged km23 and Flag-tagged km23-2 (top panel, lane 2). Specificity of the immunocomplex is demonstrated by the antibody control shown in lane 1 (top panel). Controls for the expression of km23-V5 were verified by Western blotting whole cell lysates using an anti-V5 antibody (bottom panel, lane 2). (c) Sedimentation coefficient distributions for 0.3 mM km23 in 25 mM sodium acetate at pH 6.0 and 20 °C as a function of urea concentration (molar concentrations of urea are designated on the left side of each distribution). Sedimentation coefficient distributions were obtained with the $C(s)$ method[35] as implemented in UltraScan.[51] Increasing urea concentration causes a shift in the sedimentation coefficient consistent with the transition from homodimer to monomer.

both km23-V5 and km23-Flag were co-transfected (top panel, lane 3). In contrast, there was no detectable immunocomplex when cells were co-transfected with km23-V5 and EV (top panel, lane 2), a result attributable to the absence of km23-Flag as immunoblot analysis revealed that km23-V5 was expressed (bottom panel, lane 2). There was also no immunocomplex apparent when normal mouse immunoglobulin G (IgG) was used as the IP antibody (top panel, lane 1), thereby demonstrating the specificity of the IP antibody. The same type of analysis was carried out to determine whether km23 might form oligomeric complexes with km23-2, the other mammalian km23 isoform that shares 77% sequence identity with km23. This was accomplished by co-transfecting 293T cells with km23-V5 and km23-2-Flag and by carrying out IP/blot analyses as before. These results, shown in Figure 1(b), revealed that km23-V5 and km23-2-Flag indeed formed detectable immunocomplexes when the anti-Flag antibody (top panel, lane 2) but not the normal mouse antibody (top panel, lane 1) was used for the IP. These results, taken together, indicate that km23 forms homo-oligomers or hetero-oligomers with km23-2 *in vivo*.

km23 forms homodimers *in vitro*

The objective of the studies described here was to use sedimentation velocity analytical ultracentrifugation to determine whether the oligomeric complexes of km23 demonstrated through the cell-based experiments corresponded to that of a dimer, similar to that of the MglB family p14:MP1 dimer, or whether km23 formed higher-order oligomeric structures. To accomplish this, a structurally homogenous form of km23 was isolated by expressing the protein, together with an artificial 20 residue N-terminal segment encoding a hexahistidine tag, in *Escherichia coli*. The protein was then purified to homogeneity using immobilized metal affinity chromatography.

The sedimentation experiments were carried out by preparing recombinant km23 (116 residues, 13.1 kDa) at a concentration of 0.3 mM in 25 mM sodium acetate at pH 6.0 containing 0.0, 1.0, 2.0, 2.3, 2.6, and 3.0 M urea. The velocity profiles were then obtained by recording the absorbance at 280 nm as the samples were centrifuged at 20 °C. The resulting data were analyzed by both the $C(s)$ method[35] and by finite element analysis with a single ideal species.[36] The results of the $C(s)$ analysis, shown in Figure 1(c), revealed single narrow peaks with mean average sedimentation coefficients that decreased from 2.1×10^{-13} to 1.9×10^{-13} s over the range from 0 M to 2 M urea and from 1.9×10^{-13} to 1.1×10^{-13} s over the range from 2 M to 3 M urea. The sedimentation coefficients ($s_{2O,W}$) and frictional ratios (f/f_o) obtained from the $C(s)$ method are listed in Table 1. These correlate closely with the corresponding values obtained using finite elements analysis (which are also listed in Table 1).

The $s_{2O,W}$ and f/f_o values obtained from the 0–2 and 3 M urea samples translate into molecular masses of 20–23 kDa and 10.5–11.1 kDa, respectively (Table 1). This suggests that km23 forms a stable homodimer in solution and that only under the strongly denaturing conditions of 2.3 M urea and higher does it begin to dissociate to yield appreciable amounts of monomer. The fact that the km23 homodimer dissociates at urea concentrations

Table 1. Sedimentation velocity analysis of km23 as a function of the urea concentration

	C(*s*) Analysis[a]			Finite element analysis[a]		
[Urea] (M)	$\overline{s_{20,w}}$ ($\times 10^{-13}$ s^{-1})	Frictional ratio (f/f_o)	$\overline{MW}$ (kDa)	$\overline{s_{20,w}}$ ($\times 10^{-13}$ s^{-1})	Frictional ratio (f/f_o)	$\overline{MW}$ (kDa)
0.0	2.03	1.33	21.0	1.98	1.44	22.6
1.0	1.98	1.57	25.9	1.81	1.48	22.5
2.0	1.77	1.46	19.7	1.80	1.41	21.6
2.3	1.74	1.47	19.2	1.74	1.42	18.3
2.6	1.63	1.49	17.9	1.63	1.43	16.7
3.0	1.24	1.43	11.1	1.23	1.38	10.5

[a] Sedimentation coefficients, weight average molecular weights, and frictional ratios are as determined with the *C*(*s*) analyses[35] and the finite element analysis[36] as implemented in the UltraScan software.[51]

comparable to that at which many small globular proteins unfold indicates that the homodimer is stabilized by an extensive array of contacts similar in nature to those that stabilize globular proteins. These conclusions have been borne out by the structural analysis of km23 by NMR as discussed below.

NMR assignments

To define the tertiary and quaternary structure of km23, NMR spectroscopy was used. Towards this end, an ^{15}N isotopically labeled sample was prepared using the *E. coli* expression and purification procedure described above. This sample was then analyzed by recording a ^{1}H–^{15}N shift correlation heteronuclear single quantum coherence (HSQC) spectrum under non-denaturing conditions (25 mM sodium acetate, pH 6.0) at 20 °C where km23 was shown through analytical ultracentrifugation to be homodimeric. The HSQC revealed a well-dispersed pattern characteristic of a structurally ordered protein, although the total number of identifiable signals corresponding to backbone amides was fewer than that anticipated based upon the primary sequence (95 observed, 109 expected). This indicated that either the dimer is relatively weak and that the signals of monomeric and dimeric forms undergo fast exchange, or that the dimerization is relatively tight and that the signals of monomeric and dimeric forms undergo slow exchange (but that only signals of the dimeric form are present). To distinguish these possibilities, ^{1}H–^{15}N HSQC spectra were recorded in the buffer described above as the sample was diluted from 1.0 mM to 20 μM. There were no detectable changes in peak positions over this 50-fold concentration range, suggesting that km23 forms a tight dimer with the signals from the monomeric and dimeric forms falling in the slow exchange regime.

The sequence-specific backbone and side-chain resonance assignments of km23 were obtained by collecting three-dimensional triple resonance NMR data sets using 0.4–0.8 mM ^{13}C,^{15}N km23 samples. The solution conditions used for the assignments were those described above (25 mM sodium acetate, pH 6) although a higher temperature was used (42 °C) to optimize sensitivity. The HSQC pattern was not changed at 42 °C relative to that at 20 °C, indicating that the higher temperature had little or no effect upon formation of the dimer.

The triple-resonance data sets enabled assignment of the backbone and side-chain resonances of all but one residue (N36) in the region corresponding to km23 (designated residues 1–96) (Figure 2). The triple-resonance data in contrast enabled the assignment of only five of the 20 residues in the N-terminal segment derived from the vector (designated residues −20 to −1). Three of the five backbone amides assigned in this region (G(−8), V(−6), and G(−3)) were further shown to be of low intensity (Figure 2). These observations suggest that the inability to assign resonances in the N-terminal region is a consequence of rapid amide exchange, which is not surprising in the light of the expected random coil nature of this region. The underlying reason for our inability to assign N36 is not clear, although one possibility is exchange broadening.

Secondary structure

The secondary structure of km23 was determined from the pattern of short-range and medium-range nuclear Overhauser effect (NOE) connectivities observed in the 3-D ^{15}N and ^{13}C-edited NOESY spectra and the consensus chemical shift index (CSI).[37] Together, these data revealed the presence of five β-strands, β1 (17–24), β2 (29–32), β3 (66–73), β4 (76–82), and β5 (86–92) and two α-helices, α1 (2–10) and α2 (36–60). The β-strand regions are supported by weak or medium $d_{N-N}(i,i+1)$ and strong $d_{\alpha-N}(i,i+1)$ NOE connectivities and a positive consensus CSI. The α-helical regions are supported by strong $d_{N-N}(i,i+1)$, weak $d_{\alpha-N}(i,i+1)$, and medium-to-weak $d_{\alpha-N}$ $(i,i+3)$ NOE connectivities and a negative consensus CSI. The pairing of the five β-strands in an antiparallel fashion is supported by numerous H^{α}–H^{α}, H^{N}–H^{α}, and H^{N}–H^{N} long-range NOEs.

Tertiary structure

There were a significant number of NOEs involving protons on residues 38, 42, 45, and 49 on the N-terminal end of α-helix 2 with protons on residues 53, 56, and 60 on the C-terminal end of

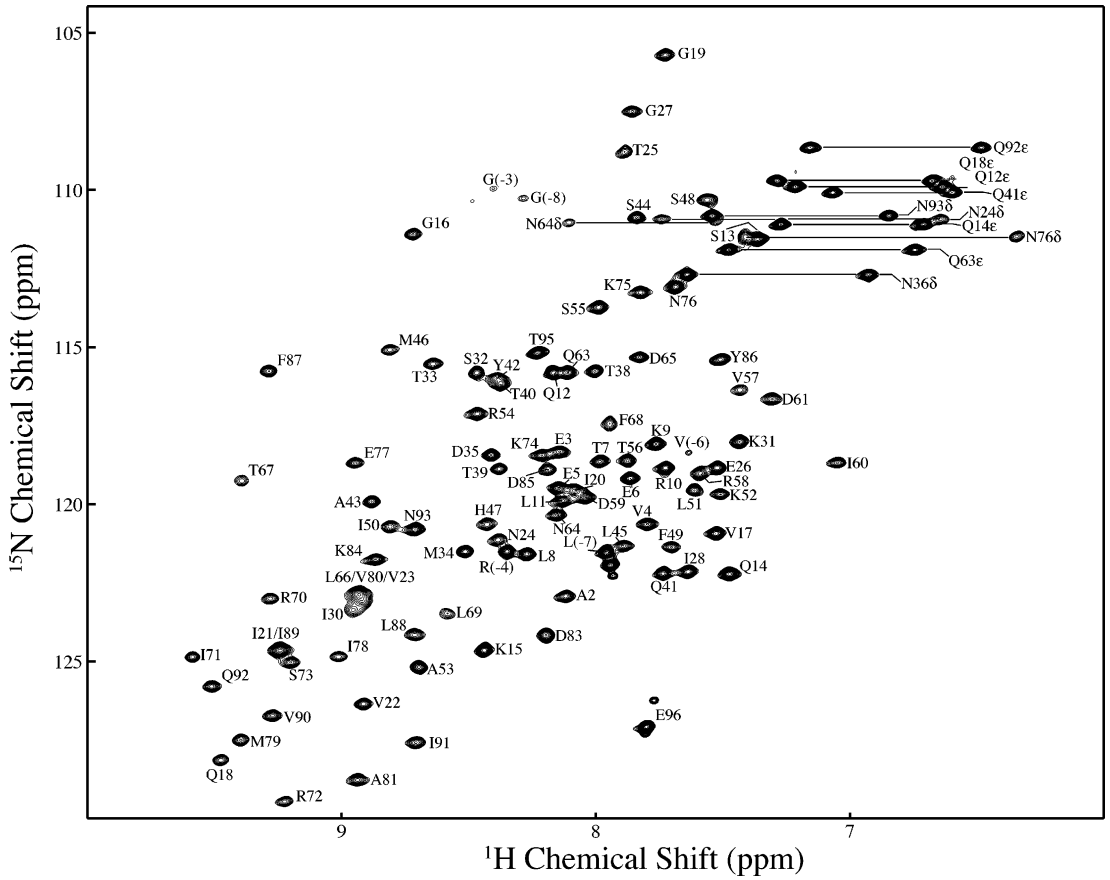

Figure 2. Two-dimensional ^{1}H–^{15}N HSQC spectrum of 0.5 mM ^{15}N km23 in 25 mM sodium acetate, 0.02% sodium azide (pH 6.0) recorded at 42 °C at a magnetic field strength of 14.1 *T* (600 MHz ^{1}H). Peaks are labeled according to their resonance assignments (numbers shown in parentheses correspond to those in the 20 residue N-terminal tail and are numbered −20 to −1; residues numbered 1 to 96 correspond to the 96 residues of human km23).

α-helix 2. These NOEs, when included in the structure calculations, required a bend in the helix near residues 51 and 52. This seemed unlikely since the $^{3}J_{HNH\alpha}$ couplings in α-helix 2 were found to range between 2.5 to 4.5 Hz, consistent with canonical helical phi values, −40° to −65°, but not with the phi values of residues 51 and 52, which fell between −80° and −90° and which had predicted $^{3}J_{HNH\alpha}$ couplings of 6.5 to 7.8 Hz. In addition, there were a number of NOEs observed between protons on residues 67, 68, and 69 on the N-terminal end of β-strand 3 with protons on residues 71, 72, and 73 of the C-terminal end of the strand. These NOEs similarly required a bend, this time at residue 70. This again seemed unlikely since the $^{3}J_{HNH\alpha}$ couplings in this region were found to range between 6.8 to 7.2 Hz, consistent with phi values characteristic of β-strand, −88° to −90°, but not with the phi value of residue 70, which was −150° and which had a predicted $^{3}J_{HNH\alpha}$ coupling of 9.2 Hz. These observations, together with the analytical ultracentrifugation results, suggest that the intra-helix and intra-strand NOEs thus observed correspond to intermolecular NOE contacts in the context of a km23 homodimer. To ascertain this, a km23 sample was prepared by mixing equivalent amounts of unlabeled and ^{13}C,^{15}N labeled km23 in denaturant (6 M urea) and by dialyzing the sample back into non-denaturing NMR buffer. Then, 3-D ^{12}C-filtered,^{15}N-edited and 3-D ^{12}C-filtered,^{13}C-edited NOESY experiments were recorded. These data sets revealed a total of 40 intermolecular contacts. The majority of these were, as anticipated, between residues on the N-terminal half of α-helix 2 or β-strand 3 of one subunit with residues on the C-terminal half of α-helix 2 or β-strand 3 of the other subunit, respectively. The observation of such NOEs unambiguously showed that km23 forms a stable homodimer in solution. These NOEs also show that the homodimer interface is formed by arranging α-helix 2 and β-strand 3 from each monomer in an antiparallel manner as in the p14/MP1 heterodimer.[33,34]

The three-dimensional structure of the km23 homodimer was then calculated using the distance geometry-simulated annealing protocol in torsion angle space as implemented in X-PLOR-NIH.[38] The structure was initially calculated using 1121 NOE and 140 chemical shift derived dihedral angle (TALOS[39]) restraints alone (Table 2). The overall fold thus obtained was consistent with expectations regarding the antiparallel arrangement of α2 and β3

noted above. To validate the structure, $^{1}D_{\mathrm{NH-HN}}$, $^{1}D_{\mathrm{C\alpha H\alpha}}$, $^{1}D_{\mathrm{C\alpha C'}}$, $^{1}D_{\mathrm{NC'}}$ and $^{2}D_{\mathrm{HNC'}}$ residual dipolar couplings (RDCs) were measured using km23 samples in a solution containing 10 mg ml^{-1} Pf1 phage.[40] The 333 RDCs thus measured were then compared to those calculated from the NMR structure using the program PALES.[41] This revealed a correlation coefficient (r^2) of 0.71 between the experimental and calculated RDCs, which is typical of NMR structures refined without the use of RDCs.[42] The structures were then further improved by including the 333 RDCs, as well as 66 $^{3}J_{\mathrm{HNH\alpha}}$ couplings, as restraints in the calculation (Table 2).

The stereoview of the ensemble of calculated structures consistent with the experimental NOE, chemical shift derived dihedral, $^{3}J_{\mathrm{HNH\alpha}}$ coupling, and RDC restraints is shown in Figure 3(a). The ensemble of structures shows excellent precision (0.53 Å for backbone atoms in regular elements of secondary structure) and low overall energies (Table 2). The analysis of stereochemical quality by the program PROCHECK[43] revealed that on average 98% of the residues lie in the most favored or additionally allowed regions of the Ramachandran plot (Table 2). Those that fall in the disallowed region correspond to S13, K15, D35 and K84. These unfavorable geometries are likely due to the fact that each of these residues fall within loops (Figures 3(b) and 5) and are poorly restrained. A ribbon diagram depicting the energy-minimized average structure is shown in Figure 3(b). The overall fold of the monomer consists of two α-helices (α1-α2) and a five stranded antiparallel β-sheet (β1–β5) connected by six loops (L1–L6). The helices are arranged perpendicular to one another with the shorter of the two (α1) packed against one face of the β-sheet and the longer one (α2) packed against the other. To orient α2, which is seven turns in length, the flanking strands, β2 and β3, position themselves as the outermost strands, while the remaining strands, β1, β4 and β5, position themselves as inner strands. The ten-stranded antiparallel β-sheet of the homodimer, which is formed by the simultaneous arrangement of α2 and β3 in an antiparallel manner, is rectangular in shape with α2 placed along the diagonal. The side of the β-sheet upon which the α2 packs is relatively smooth and convex in shape. In contrast, the side of the β-sheet upon which α1 packs has a major depression formed by the space between the two N-terminal

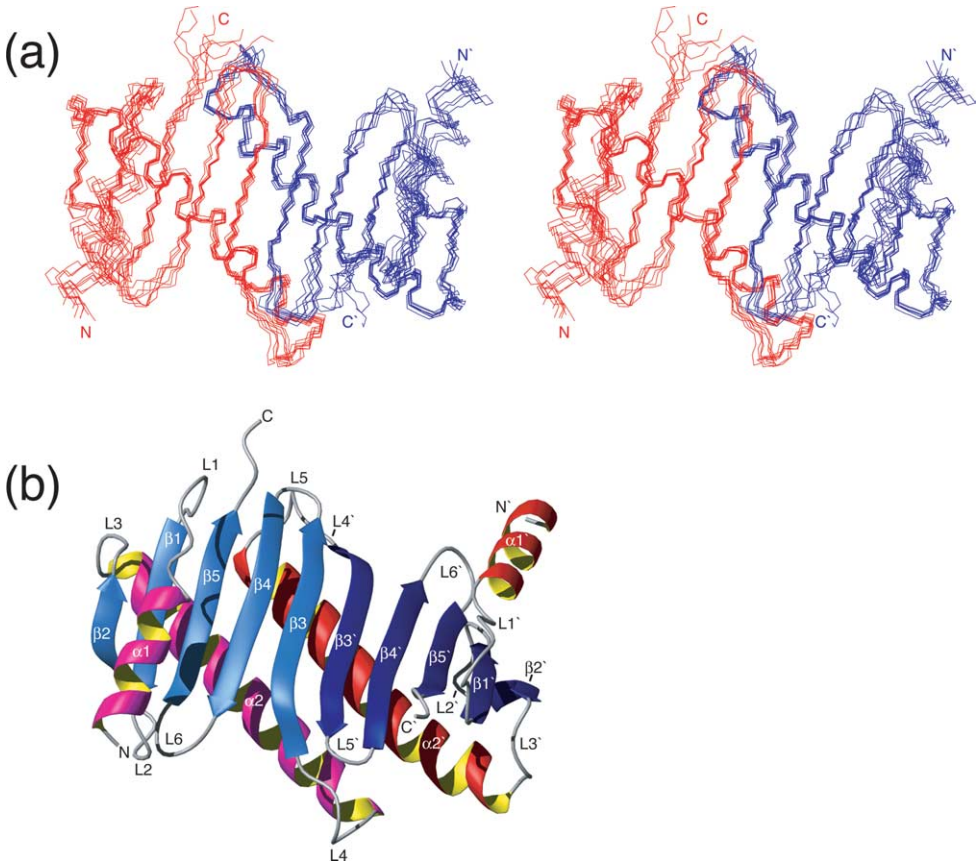

Figure 3. Solution structure of homodimeric km23. (a) A stereoview of the ensemble of eight lowest-energy structures superimposed on the basis of the deduced secondary structure, α1 (2–10), β1 (17–24), β2 (29–32), α2 (36–60), β3 (66–73), β4 (76–82), β5 (86–92). Monomers are colored red and blue. (b) Ribbon diagram of the km23 homodimer in which the regular elements of secondary structure are identified. Monomers are distinguished based upon the shading of the β-strands and α-helices (monomer 1, dark blue β-strands and red/yellow α–helices; monomer 2, light blue β-strands and magenta/yellow α-helices).

Table 2. Structural statistics for km23

Restraints		Experimental
Total restraints		1660
NOE distance restraints		
Intraresidue ($\|i-j\|=0$)		273
Sequential ($\|i-j\|=1$)		384
Short range ($2\leq\|i-j\|\leq5$)		214
Long range ($\|i-j\|>5$)		210
Intersubunit		40
Dihedral restraints		
ϕ		70
ψ		70
RDC restraints		
$^1D_{NH}$		63
$^1D_{C\alpha H\alpha}$		54
$^1D_{C\alpha C'}$		82
$^1D_{NC'}$		67
$^{2-}D_{HNC'}$		67
Coupling restraints		
$^3J_{HNH\alpha}$		66
Deviation among ensemble		
Bonds (Å)		0.0033±0.0003
Angles (degrees)		0.85±0.03
Impropers (degrees)		0.87±0.095
Dihedral restraints (degrees)		2.4±0.8
RDC (Hz)		
$^1D_{NH}$		1.0±0.1
$^1D_{CH}$		2.1±0.1
$^1D_{C\alpha CO}$		3.9±0.2
$^1D_{NC'}$		2.6±0.1
$^{2-}D_{NHC'}$		3.8±0.2
$^3J_{HN\alpha}$ restraints (Hz)		0.7±0.1
Ramachandran plot[a]		
Most favored (%)		79.1
Additionally allowed (%)		18.6
Generously allowed (%)		0.0
Disallowed (%)		2.3
Overall precision		
Secondary structure	Backbone[b]	0.53
	Heavy[b]	0.98
Ordered residues[c]	Backbone[b]	0.74
	Heavy[b]	1.25

Structural statistics are calculated for the ensemble of eight lowest energy structures.
[a] Calculated using the program PROCHECK.[43]
[b] Backbone atoms include N^H, C^α, and C^O; heavy includes all non-hydrogen atoms.
[c] Ordered corresponds to residues 21–112.

α-helices. This surface of the molecule, as discussed below, includes a number of solvent-exposed residues conserved among sequences from different species.

km23 dynamics

The internal flexibility of km23 has been investigated by measuring ^{15}N T_1, ^{15}N T_2, and ^{15}N-{^1H} NOE relaxation parameters at two magnetic field strengths (14.1 and 16.4 *T*). The raw relaxation data were analyzed to first determine the extent of diffusional anisotropy, which is important, as anisotropies as small as 1.2 have been shown to interfere with interpretation of relaxation data using the model-free formalism.[44]

To assess the extent of diffusional anisotropy for km23, the experimental T_1/T_2 data were fit to a diffusional model with axial symmetry.[45] The χ^2 value, which provides an indication of the agreement between the experimentally measured and modeled T_1/T_2 data, was found to be 6.7 and 4.4 for the data collected at 14.1 and 16.4 *T*, respectively (Table 3). These χ^2 values were lower than the corresponding ones obtained for the fit to an isotropic model (12.6 and 10.6 for the data collected at 14.1 and 16.4 *T*, respectively), indicating that km23 indeed tumbles anisotropically. To demonstrate that the improvement was specifically due to diffusional anisotropy, the experimental T_1/T_2 data were again fitted to an anisotropic model but with randomized N–H bond vector orientations. The χ^2 values obtained in this case ($\chi^2=11.8$ and 10.0 for the data collected at 14.1 and 16.4 *T*, respectively) (Table 3) were reduced relative to the values obtained with the isotropic model, but not nearly to the same extent as for the fit to the axially asymmetric model with non-randomized N–H bond vector orientations. The significance of the fit was further shown by the correspondence of the fitted parameters to those estimated from the calculated inertia tensor. Thus, the orientation of the principal axis of the experimentally fitted diffusion tensor, defined by the polar angles ϕ and ψ (Table 3A), agreed closely with ϕ and ψ values that define the principal axis of the calculated inertia tensor (Table 3B). The experimental estimates for the extent of anisotropy, $D_\parallel/D_\perp$ (Table 3A), also agreed with estimates based on the calculated inertial anisotropy (Table 3B). These observations are consistent with both that of the fitted tensor and the homodimeric structure of km23, as inertial calculations carried out on monomeric km23 predict a much lower degree of anisotropy ($D_\parallel/D_\perp=1.05$) and a principal axis that runs parallel to that of the β-strands, rather than perpendicular, as in the case of homodimeric km23.

The experimental T_1/T_2 data collected at the two different magnetic field strengths were also modeled assuming full diffusional asymmetry.[46] The χ^2 values in this case were slightly lower than those obtained by fitting to an axially symmetric model (5.8 and 3.7 for the data collected at 14.1 and 16.4 *T*, respectively). These fits, however, were not considered statistically significant, as the fitted parameters for the diffusion constants along the minor axes did not differ in a statistically significant way. This is consistent with the small degree of inertial anisotropy along the minor axes ($I_{yy}=1.80\pm0.07$ and $I_{zz}=2.01\pm0.06$) (Table 3B) and shows that the km23 homodimer is best described by an axially symmetric, not a fully asymmetric, diffusion tensor.

Model-free analyses were performed with the axially symmetric tensor described above using the program ModelFree4.[47] The model-free fits were carried out by simultaneously fitting the experimental relaxation data collected at the two magnetic field strengths using the procedure described by Mandel.[47] This yielded statistically significant fits for all residues, except L45, A81, T95 and E96. The S^2, τ_e, and R_{ex} values derived in this

Table 3. Modeling of the km23 diffusion tensor

A. *Experimental axially symmetric diffusion tensor*

Field	NH vectors	θ (degrees)	ϕ (degrees)	$D_{\|}/D_{\perp}$	τavg (ns)[a]	χ^{2} [b]
16.4 T	Experimental[c]	90.3±1.9	8.4±2.0	1.58±0.04	9.82±0.07	4.4±0.5
16.4 T	Random[d]	91.4±34.7	113.3±63.7	1.14±0.14	10.06±0.12	10.0±0.4
14.1 T	Experimental	90.3±3.9	11.3±2.7	1.68±0.06	9.53±0.03	6.7±04
14.1 T	Random	130.1±30.0	70.8±45.2	1.21±0.06	9.86±0.10	11.8±0.4

B. *Modeled axially symmetric diffusion tensor*[e]

I_{xx}	I_{yy}	I_{zz}	θ (degrees)	ϕ (degrees)	$D_{\|}/D_{\perp}$
1.00±0.00	1.80±0.07	2.01±0.06	89.3±0.1	−0.6±1.1	1.45±0.03

[a] The average correlation time defined according to the convention described by Woessner.[78]
[b] Normalized value of chi squared defined according to Tjandra.[45]
[c] NH bond vector orientations were calculated from the ten lowest energy km23 homodimer structures.
[d] NH bond vector orientations were calculated from the ten lowest energy km23 homodimer structures, but then randomized with respect to residue number.
[e] Euler angles (θ, ϕ) are based upon the calculated inertia tensor from the ten lowest energy km23 structures. Diffusional anisotropy, $D_{\|}/D_{\perp}$, is derived from the calculated inertia tensor from the ten lowest energy km23 homodimer structures using the relation $D_{\|}/D_{\perp} = [0.75(2(I_{\perp}/I_{\|})-1)]^{1/2}$.

manner are plotted in Figure 4. As shown, most residues exhibit S^2 values greater than 0.85, indicating that the backbone is relatively rigid on the ns to ps time-scale, although there are a few exceptions as shown by moderately decreased S^2 values and higher τ_e values for residues located near the N terminus (A2, E3 and V4) and in two loops (S13 and G16 in L1 and D85 in L6) (Figure 4). There are also residues that undergo motions on the ms to μs time-scales as satisfactory model-free fits of

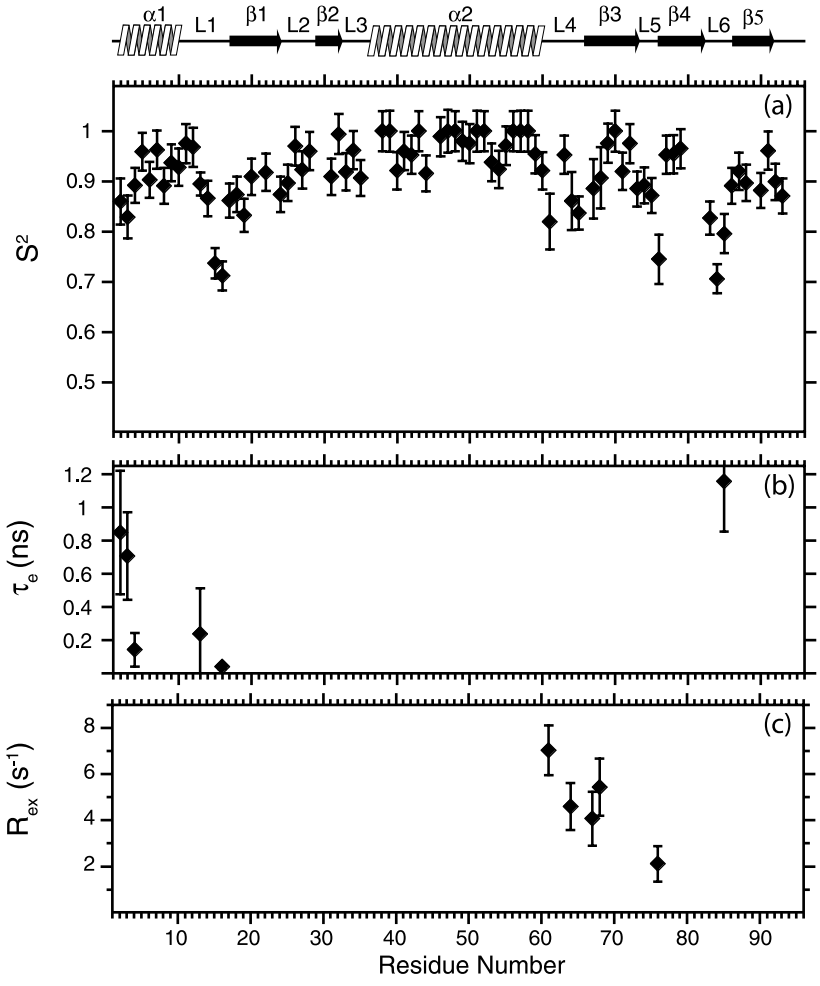

Figure 4. Model-free parameters for km23 backbone amides derived by simultaneous fitting of ^{15}N T_1, ^{15}N T_2, and ^{15}N-{^{1}H} NOE data recorded at magnetic field strengths of 14.1 and 16.4 *T*. The modeling was carried out using an axially symmetric diffusion tensor with $D_{\|}/D_{\perp}=1.63$, $\tau_{avg}=9.68$ ns, and N–H bond vector information derived from the average of the lowest energy km23 structures. Lipari-Szabo S^2, τ_e, and R_{ex} parameters are shown in (a), (b), and (c), respectively. Data points not shown for specific residues in (b) and (c) indicate that this parameter was not included in the motional model for that residue.

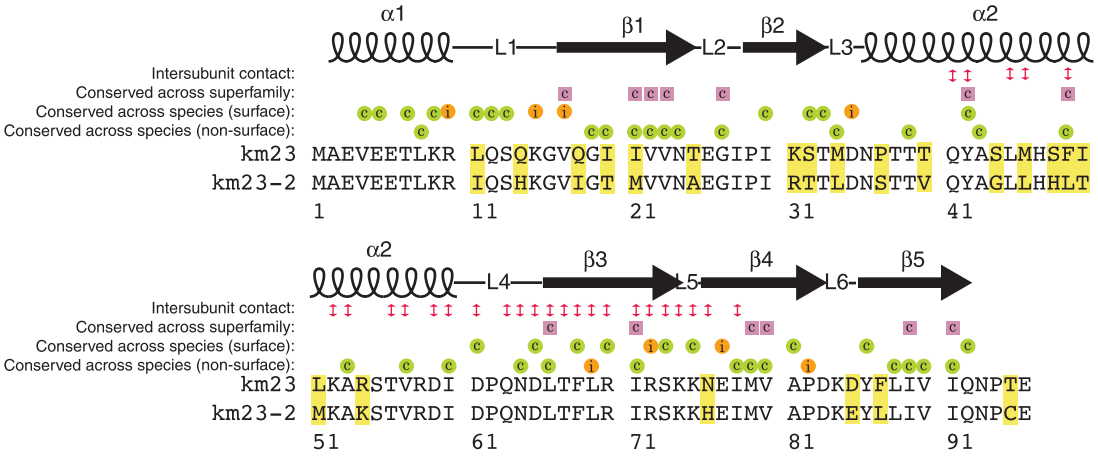

Figure 5. Conservation of km23 isoforms. Residues conserved across the MglB/robl superfamily are designated by purple squares with the letter c. Residues that are either invariant or conserved relative to that of km23 from different species are indicated by orange or light green circles with the letters i and c, respectively (surface and non-surface residues are distinguished based on their side-chain solvent accessible surface areas; those with greater than 40% exposure are considered surface; those with less than 40% exposure are considered non-surface). Residues that differ between human km23 and human km23-2 are shaded yellow. Residues that lie at the km23 homodimer interface are indicated by double-ended red arrows. Sequences used in the determination of the conservation across the MglB/robl superfamily were the 54 reported by Koonin and Aravind.[32] Sequences used in the determination of conservation of km23 across species were obtained from NCBI and included *H. sapiens, R. norvegicus, M. musculus, C. familiaris, G. gallus, D. rerio, C. reinhardtii, D. melanogaster, C. elegans, C. briggsae, S. similes, G. lamblia, A. gambiae, C. intestinalis, and T. nigrovirdis*. Sequence conservation was assessed using the program AMAS[49] with a conservation threshold of 7.

the relaxation data required non-zero R_{ex} terms for five residues. These are clustered in loop L4 (D61, N64, T67 and F68) as shown (Figure 4).

Discussion

Homodimeric nature of km23 provides a structural paradigm for the MglB/robl superfamily

The analytical ultracentrifugation and NMR experiments described here have shown that km23 is homodimeric in solution and that the dimerization is mediated by the simultaneous pairing of the edge β-strand (β3) of a five-stranded antiparallel β-sheet and by a seven turn α-helix (α2) that lies diagonally across the surface of the sheet. The interfacial contact is extensive, with each of the monomers burying 1255 Å^2 of solvent accessible surface at the interface. The residues that participate in the interface are 60% hydrophobic and 40% charged or polar (Figure 5, red double-ended arrows). The hydrophobic residues generally exhibit a low degree of solvent accessibility (8.6% on average) and are located mostly along α-helix 2 or β-strand 3. Those along α-helix 2 pack against the underlying β-sheet, whereas those along β-strand 3 pack against residues from β-strand 3 of the other monomer. The charged and polar residues generally exhibit a higher degree of solvent accessibility (29.2% on average) and are found both within the secondary structures that form the interface (α2 and β3), as well as in the connecting loops that approach one another at the interface (loop 4 from one monomer and loop 5 from the other monomer; see Figure 3(b)). The charged or polar residues found within α2 (Q41, K52, and D59) or β3 (R70 and R72) invariably exhibit a high degree of solvent accessibility and therefore are not likely important in terms of either stabilizing the dimer or in determining the specificity of the monomer-monomer pairing. The charged or polar residues in the connecting loops (D61, Q63, N64, and D65 in loop 4 and R70 and R72 in loop 5) exhibit a lower degree of solvent accessibility and engage one another through ion pairs (loop 4 D61–loop 5′ K75 and loop 4 D65–loop 5′ K74) and several side-chain–side-chain and side-chain–backbone hydrogen bonds. Thus, in contrast to the polar and charged residues noted above, those in loops 4 and 5 are likely important both in stabilizing the dimer and contributing to the specificity of the monomer-monomer pairing.

The km23 homodimer as noted is similar in architecture to the heterodimer formed between the MglB family proteins, p14 and MP1.[33,34] The structural similarity between the two dimers, as indicated by the RMSD in backbone atom positions of residues within the β1–β2–α2–β3–β4–β5 structural core, is 1.4 Å (Figure 6(a)). The largest structural difference between the two dimers involves the N-terminal α-helix (α1), which in km23 is positioned such that it initiates above the N-terminal end of β-strand 5 and proceeds in a direction parallel to that of the underlying strands, whereas in p14 it initiates above the N-terminal end of β-strand 2 and proceeds diagonally across the strands (Figure 6(b)). This change enables the

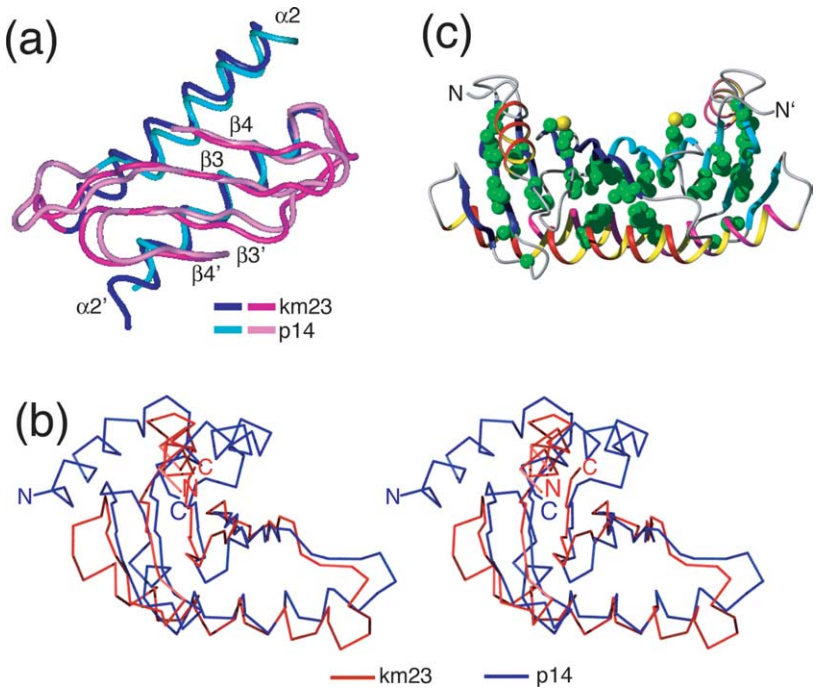

Figure 6. Structural comparison of the km23 homodimer with the crystal structure of the p14:MP1 heterodimer.[33] (a) An overlay of backbone ribbons of the km23 homodimer and p14:MP1 heterodimer in the region of the dimer interface. Region shown includes the interfacial α-helix and β-strand (α2 and β3, respectively) together with the flanking β-strand (β4). Ribbon corresponding to km23 is depicted in dark blue and magenta; ribbon corresponding to p14:MP1 is depicted in light blue and pink. (b) An overlay of C^{α} traces of the km23 monomer (red) and the p14 component of the p14:MP1 heterodimer (blue) shown in stereo. Structures were aligned by minimizing the deviation between the backbone atom positions of β1, β2, α2, β3, β4, and β5. km23 and p14 are shown to share a conserved arrangement of β1, β2, α2, β3, β4, and β5, but differ in that p14 includes a C-terminal α-helix, whereas km23 does not. km23 and p14 also differ in that the N-terminal helix lies nearly parallel with the underlying β-strands in km23, whereas in p14, the helix lies at an approximate 30 degree angle such that the N terminus is positioned close to β-strand 3 near the center of the dimer interface. (c) A ribbon diagram of the km23 homodimer (rotated by +90 degrees around the *x*-axis relative to that shown in Figure 3(b)) in which the side-chains of residues conserved among all known members of the MglB/robl superfamily are displayed. Residues included are V17, I20, I21, V22, G27, A43, F49, L66, I71, M79, V80, I89, and I91. Residues cluster in the area between the central ten-stranded antiparallel β-sheet and the α-helices (α1, α2) that pack against it. Ribbon is shaded such that the strands and helices from one monomer are dark blue and red/yellow, respectively, while those from the other monomer are light blue and magenta/yellow, respectively. Side-chains are displayed in CPK format with carbon atoms shaded green and sulfur atoms shaded yellow.

C-terminal α-helix, which is present in MglB, but not robl family members, to pack against the N-terminal α-helix without overlapping with the C-terminal helix from the other monomer.

The other feature that the p14:MP1 heterodimer and the km23 homodimer share in common is the fact that both form tight dimers. This has been directly shown in the case of the p14:MP1 heterodimer through the determination of the p14:MP1 dissociation constant ($K_d = 13$ nM) using surface plasmon resonance.[34] The K_d of the km23 monomers for one another has not been determined directly, although we estimate it to be about 10 nM or lower. This estimate is based on a dissociation rate constant (k_{off}) of about 5 s^{-1} or slower and an association rate constant (k_{on}) of 5×10^8 M^{-1} s^{-1}. The value for k_{off} is based upon the experimental observation of high intensity positive NOEs in the filtered NOESY experiments, which would only occur if the disassociation rate constant was slower than the inverse of the NOE mixing time (120 ms). The value for k_{on} is based upon the assumption that association is diffusion-controlled and that it occurs according to the translational rate constants determined from the sedimentation velocity analytical ultracentrifugation experiments in the absence of urea.

The high degree of structural similarity between these two dimers is rather remarkable given that their primary sequences are relatively poorly conserved (km23 exhibits 32% and 30% conservation relative to MP1 and p14, respectively, when residues at structurally equivalent positions are compared). The residues that are conserved between these proteins and other members of the MglB/robl superfamily are indicated in Figure 5 (purple squares with the letter c). These conserved residues are largely hydrophobic, and as illustrated in Figure 6(c), lie principally at the interface between the central ten-stranded β-sheet and α-helices 1 and 2 that pack on either side. These observations, together with the high stability of the two dimers that have been studied, suggest that all members of the MglB/robl superfamily adopt and function in the context of such dimeric structures. The significance of this is not yet clear, although one possibility, as suggested in the case of the p14:MP1 heterodimer, is to enable binding to multiple partners *via* distinct interactions through each of the monomeric subunits.[33,34] The significance of this in the case of homodimers is less clear, although one possibility as discussed below in the context of the km23 homodimer, may be to enhance affinities for binding *via* avidity effects.

Conserved surfaces and potential binding sites for Smad and DIC

The DIC binding function of km23 has been demonstrated previously.[10] km23 has also been shown to be serine-phosphorylated after TGFβ receptor activation[10] and to be partially required for TGFβ-mediated effects on both fibronectin expression and cell cycle progression.[10,28,48] The emerging picture from these findings is that TGFβ signaling leads to the phosphorylation of both Smad2 and km23 and that phosphorylated km23 plays an essential role in the dynein-mediated transport of Smad2 to the nucleus.[48] km23 may therefore bind TβRII, Smad2, and DIC, and such binding, as in the case of the DIC, may be regulated *via* phosphorylation.

To identify potential protein binding sites on the surface of km23, we analyzed the location of surface residues that are either invariant or conserved among km23 sequences from different species. The invariant and conserved residues were identified by aligning km23 sequences from different species and by assessing conservation using a flexible set-based method as implemented in the program AMAS.[49] The criterion used to distinguish surface residues from non-surface residues was based on the calculated residue-specific side-chain solvent accessible surface areas (the cutoff was set at 40%; those residues with greater than 40% solvent accessible surface areas were considered surface; those with less than 40% solvent accessible surface areas were considered non-surface). The invariant and conserved residues identified in this manner are indicated in Figure 5 (orange circles with an i and green circles with a c, respectively) and their location on the surface of the km23 homodimer is shown in Figure 7(a). The most striking feature is that the invariant (shaded red) and the conserved residues (shaded either green or yellow depending upon whether they are serine or non-serine, respectively) map to the face of the molecule and to the adjacent edge that includes the N-terminal α-helices (middle and left panels, respectively) but not the convex surface formed by the seven turn α-helices (right panel). The three conserved serine residues, S13, S32, and S73, are distributed amongst the invariant and conserved residues with S13 and S73 lying on the surface that includes the two N-terminal α-helices and with S32 lying on the adjacent edge. This is potentially significant as complementary biochemical studies (provided as Supplementary Data) have shown that the conserved serine residues, particularly S32 and S73, are critical sites for phosphorylation by the TGFβ receptors. Taken together, these observations

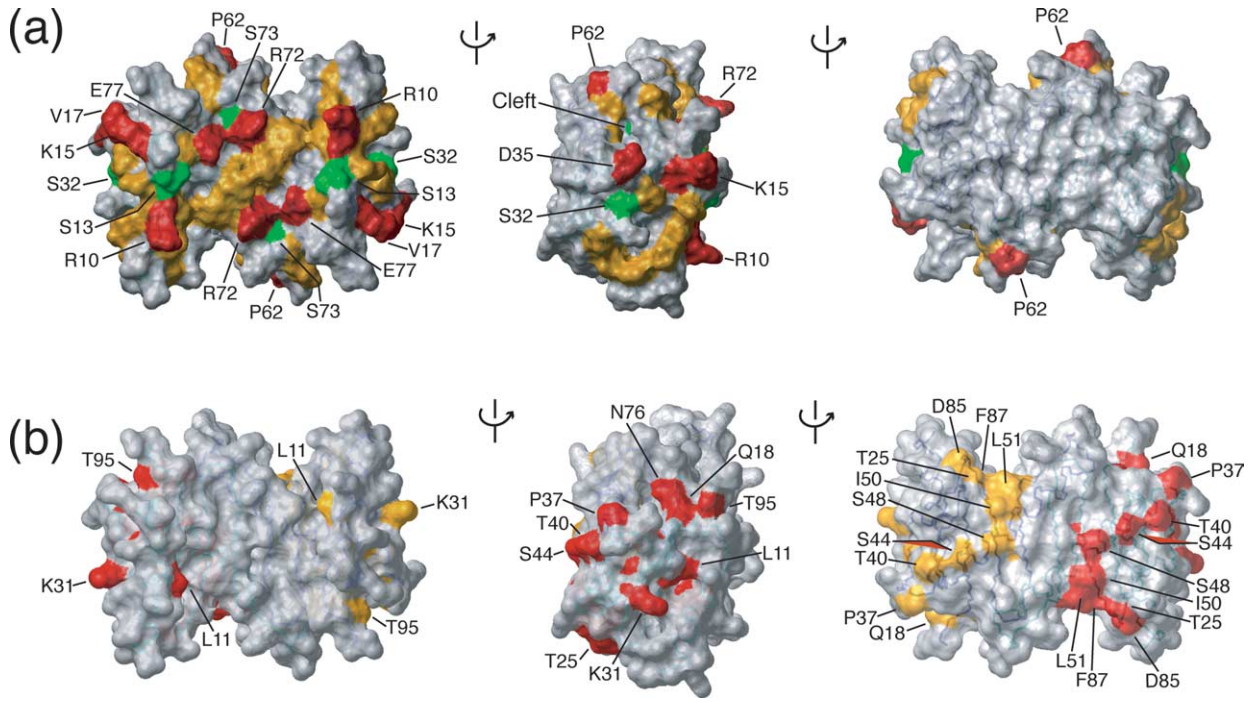

Figure 7. Potential binding sites on the surface of the km23 homodimer. (a) km23 residues that are invariant or conserved across a range of 15 different species and exhibit greater than 40% solvent exposure of their side-chains are shaded red, yellow, or green. Residues shaded red are invariant, residues shaded yellow correspond to conserved non-serine residues, and residues shaded green correspond to conserved serine residues. All other residues are shaded grey. The three surfaces shown correspond to different views of the same molecule. The view shown on the left corresponds to that shown in Figure 3(b). The other two views correspond to successive +90 degree rotations around the *y*-axis of that shown on the left. The "cleft" label designates the deep cleft formed by the incomplete overlap of loops 4 and loop 5 from opposing monomers. (b) km23 residues that differ relative to km23-2 are shaded red and yellow (the two colors correspond to whether these residues originate from monomer 1 or 2). All other residues are shaded grey. The three surfaces shown correspond to different orientations as in (a).

suggest that the surface that includes the two N-terminal α-helices may be involved in DIC binding and that phosphorylation of S32, S73, or both by the TGFβ receptors may regulate this process.

The cleft that is formed by incomplete overlap of loops 4 and 5 from the two monomers that lies adjacent to the putative DIC binding site (Figure 7(a), middle panel, labeled cleft) provides an ideal binding site for other molecules that km23 might bind, such as TβRII and Smad2. The key features of this site include its size, which is narrow (2–3 Å) and deep (11 Å), and the fact that it is lined with a number of hydrophobic residues, including A53, T56, V57, I60, and L66 from one subunit and Y42, M46, F49, I71, I78, V80, and I89 from the other subunit, all but two of which, M46 and T56, are conserved among km23 sequences from different species (Figure 5). The other interesting feature of this site includes the fact that it is flexible on both the ns-to-ps and ms-to-μs time-scales as shown by decreased order parameters (S^2) for most residues in loops 4 and 5 (Figure 4(a)) and non-zero R_{ex} terms for residues 61 and 64 in loop 4, residues 67 and 68 in the N-terminal end of β-strand 3, and residue 76 in loop 5 (Figure 4(c)), respectively. The flexibility inherent in this region of the protein is particularly intriguing, because if this indeed corresponds to the functional cargo binding site, it would provide a similar solution as to how to bind different partners using a single site as that of the LC8 DLCs.[22,27] There are clearly other possible binding modes that might utilize one of the other km23 serine residues to regulate DIC binding. There may also be as yet undetected surfaces through which km23 binds either DIC or other partners. Whatever the mechanism, the structure of the km23 presented here provides an invaluable resource with which to begin to dissect the diverse binding properties that this protein has been shown to exhibit.

km23 and km23-2 mainly differ through substitution of surface residues

The structure of the km23 homodimer presented here contributes to our understanding of the diversity of DLC subtypes in two important ways. The first is that it unequivocally establishes that the LC7/robl/km23 class of light chains is structurally distinct from that of the LC8 and Tctex classes. The LC7/robl/km23 class has an α–β–β–α–β–β–β topology with a strand order of β2–β1–β5–β4–β3, whereas the LC8 and Tctex class has an α–β–α–α–β–β–β–β topology with a strand order of β1–β4–β5–β2–β3′ (β3′ designates that β3 is from the other monomer). The two structurally distinct folds have likely arisen to enable diversification of cargo binding. The fact that both form stable homodimeric structures is curious and could be related to the fact that both bind their cargo peptides at the conformationally flexible dimer interface, as alluded to earlier. The homodimeric structures might alternatively enable tighter binding to other dimeric species through the existence of two weak non-interacting binding sites (i.e. through avidity effects). This could be important, for example, in binding and orienting km23 on the surface of the cytoplasmic domain of TβRII as homodimeric TGFβ assembles TβRI and TβRII into a heterotetrameric complex containing two type I and type II receptors. This type of binding would also be functionally advantageous, as this would ensure that km23 only binds and is phosphorylated upon ligand-induced assembly of the TβRI:TβRII tetrameric complex.

The second way in which the structure of the km23 homodimer contributes to our understanding of the diversity of light chains relates to the existence of the other mammalian homologue of km23, km23-2. km23-2 shares 77% sequence identity with km23, and as shown through the cell-based studies, forms complexes, likely heterodimers, with km23-2. There are not, as yet, any documented differences in either DIC or cargo binding properties of km23 and km23, although the two homologues have in some cases been shown to be differentially expressed.[50]

The fact that km23 and km23-2 can form a heterodimeric structure is not surprising in light of the structure presented here, since out of the 27 interfacial residues in km23, only three differ in km23-2. These include M46, F49, and N76 in km23, which are substituted to L46, L49, and H76 in km23-2 (Figure 5, red double-ended arrows). These differences are not anticipated to have a major effect on dimerization since the substitutions are, in general, conservative and since the interfacial contact area is extensive for just one of them (L49, which has an interfacial contact area of 83 $Å^2$; M46 and N76 have interfacial contact areas of just 7 and 16.5 $Å^2$, respectively).

To identify differences in potential binding properties of km23 and km23-2, we have analyzed the location of residues that differ between these isoforms, as shown in Figure 7(b) (yellow and red shading indicates whether the residues fall within the first or second monomer). The striking feature of the pattern is that it is the opposite of that shown in Figure 7(a). This suggests that residues that differ between km23 and km23-2 do not alter either DIC or cargo binding. What role then might such residue differences play? One possibility is that there may exist an as yet unidentified binding protein that differentially interacts with residues that are part of this surface to modulate function of one particular isoform over the other. One other possibility is that such differences play no real role other than accommodating the existing structure without altering either DIC or cargo binding. One way that this may have happened is through gene duplication, leading to a functionally equivalent protein with the same overall structure, but transcriptionally regulated in a distinct developmentally and tissue-specific manner. One advantage this would provide would be to regulate specific transport and/or motor regulatory activities in a manner most appropriate to individual cells and tissues.

Materials and Methods

Constructs

A construct encoding His-tagged human km23 was generated by PCR amplification of the km23 coding region and insertion into the NdeI and BamHI sites of the bacterial expression vector pET15b (Novagen, Madison, WI). The Flag-tagged km23 and km23-2 constructs were generated by inserting a PCR fragment of human km23 or km23-2 into the pFlag-CMV 5a vector (Sigma-Aldrich, St. Louis, MO) using the BglII and SalI cloning sites. The V5-tagged km23 construct was generated by cloning km23 into the pcDNA3.1/V5-His vector (Invitrogen, Carlsbad, CA) using the BamHI and XhoI cloning sites. All constructs were verified by DNA sequencing in both directions.

Expression and purification of km23

km23 protein samples were prepared by transforming the pET15b expression construct into BL21(DE3) host cells and then culturing the transformed cells on LB medium at 37 °C containing 100 μg/ml ampicillin. Protein expression was induced by the addition of 1 mM isopropyl-β-D-galactopyranoside (IPTG) when the absorbance of the cell culture at 600 nm reached 0.6–0.7. Cells were harvested three hours after induction and frozen. Cells from one liter of culture medium were resuspended in 40 ml of lysis buffer (50 mM NaCl, 20 mM Tris–HCl (pH 7.9), 5 mM imidazole, 1 mM phenylmethyl-sulfonyl fluoride, 10 μM leupeptin) and sonicated. Lysates were centrifuged at 14,000*g* for 20 minutes to remove the debris and the supernatant was filtered through a 0.45 μM membrane before loading onto a 5 ml bed of His·Bind resin (Novagen, Madison, WI) equilibrated with lysis buffer. The resin was sequentially washed with 45 ml of lysis buffer and 45 ml of wash buffer (50 mM NaCl, 20 mM Tris–HCl (pH 7.9), 60 mM imidazole) and the protein was then eluted with 30 ml of elution buffer (50 mM NaCl, 20 mM Tris–HCl (pH 7.9), 1 M imidazole). The protein was dialyzed against 25 mM sodium acetate, 0.02% sodium azide at pH 6.0 and then concentrated using a centrifugal filter with a 3000 molecular weight cutoff (VivaSciences, Palaiseau Cedex, France).

Cell culture

293T cells were purchased from American Type Culture Collection (ATCC, Rockville, MD) and were cultured in Dulbecco's Modified Eagle's Medium with glutamine supplemented with 10% (v/v) heat-inactivated fetal bovine serum. Cells were maintained in 5% CO_2 at 37 °C. Cultures were routinely screened for mycoplasma using Hoechst staining.

Immunoprecipitation/immunoblotting (IP/blot)

293T cells were transiently transfected with the indicated constructs using Lipofectamine PLUS (Invitrogen, Carlsbad, CA) following the manufacturer's protocol. 24 hours after transfection, cells were harvested using RIPA buffer (1x PBS, 1% (v/v) Nonidet P-40, 0.5% (w/v) sodium deoxycholate, 0.1% (w/v) SDS) supplemented with protease inhibitor cocktail (Roche, Indianapolis, IN). The cell lysates were incubated with 2 μg anti-V5 antibody (Invitrogen, Carlsbad, CA) for one hour at 4 °C, followed by incubation with 20 μl of Protein G-Plus agarose beads (Santa Cruz Biotechnology, Inc, Santa Cruz, CA) overnight at 4 °C. Agarose beads were washed three times with RIPA buffer and immune complexes were separated by 15% (w/v) SDS-PAGE, transferred to a PVDF membrane, and immunoblotted with an anti-Flag antibody (Sigma-Aldrich, St. Louis, MO).

Sedimentation velocity

The oligomeric state of km23 was investigated by monitoring its sedimentation properties in sedimentation velocity experiments as the urea concentration was varied. The samples used for these experiments were 0.50 ml in volume and consisted of 0.30 mM km23 in 25 mM sodium acetate (pH 6.0) with 0, 1.0, 2.0, 2.3, 2.6, and 3.0 M urea. The sedimentation velocity profiles were collected by monitoring the absorbance at 280 nm as the samples were centrifuged at 60,000 rpm and 20 °C in a Beckman Optima XL-I centrifuge fitted with a four-hole AN-60 rotor and double-sector aluminum centerpieces. Sedimentation coefficients and molecular masses were determined by fitting using both the *C*(*s*) method[35] and by finite element solutions to the Lamm equation,[36] both as implemented in UltraScan 7.0.[51] Buffer density and viscosity corrections were made using the method described by Laue *et al*.[52] as implemented in UltraScan.[51] The partial specific volume of km23 was estimated from the protein sequence as described by Cohn and Edsall.[53]

NMR samples

Samples of km23 for NMR were prepared in buffer consisting of 25 mM deuterated sodium acetate, 0.02% (w/v) sodium azide (pH 6.0) and were between 0.3 and 0.8 mM in concentration. Samples of km23 uniformly labeled with either ^{15}N or ^{15}N, ^{13}C were prepared by *E. coli* expression and purification as described above, except minimal medium with isotopically labeled growth substrates was used in place of LB medium. Samples of 10% fractionally ^{13}C labeled km23 for assignment of the side-chain methyl groups of valine and leucine were prepared by culturing the cells on minimal medium containing 0.03 g l^{-1} {^{13}C]glucose and 0.27 g l^{-1} unlabeled glucose.[54] Isotopic heterodimers of km23 were prepared by mixing an equal amount of unlabeled and ^{13}C, ^{15}N isotopically labeled km23 in 25 mM sodium acetate at pH 6.0 containing 6 M urea. The mixture was then dialyzed at 4 °C into NMR buffer and then concentrated to a final concentration of 0.6 mM.

NMR spectroscopy

All NMR experiments were performed at 42 °C on Bruker 600 MHz and 700 MHz spectrometers equipped with either conventional (700 MHz) or cryogenically cooled (600 MHz) 5 mm ^{1}H probes equipped with ^{13}C and ^{15}N decoupler and pulsed field gradient coils. All spectra were processed using NMRPIPE[55] and analyzed using the program NMRView.[56]

Resonance assignments

Backbone resonance assignments of km23 were obtained by collecting and analyzing HNCA,[57] HNCACB,[58] CBCA-(CO)NH,[59] and HNCO[60] data sets. Side-chain ^{1}H and ^{13}C assignments were obtained by collecting and analyzing (H)CC(CO)NH[61] and H(CC)HTOCSY[62] data sets. Aromatic

ring proton assignments were achieved by first recording a ^{1}H–^{13}C HSQC and a ^{1}H–^{13}C HSQC with a ^{1}H TOCSY relay using an unlabeled km23 sample. Assigned aromatic spin systems were correlated with those of the backbone through $^{1}H^{\beta}$–$^{1}H^{\delta}$ NOEs identified in a 3-D ^{13}C-separated NOESY spectrum.

Structural restraints

Intramolecular NOE distance restraints were identified through analysis of three-dimensional ^{15}N and ^{13}C-edited NOESY experiments performed using mixing times 120 ms and 200 ms, respectively. Ambiguities that arose in the assignment of amide-aliphatic NOEs in the three-dimensional ^{15}N-edited spectrum were further resolved by recording a 3-D ^{15}N-, ^{13}C-edited NOESY spectrum with a mixing time of 134 ms. Intermolecular NOEs were identified by recording 3-D ^{12}C-filtered, ^{15}N-edited and 3-D ^{12}C-filtered, ^{13}C-edited NOESY experiments[63,64] using a km23 isotopic heterodimer prepared in the manner described above. Residual dipolar couplings (RDCs) were measured by preparing ^{15}N or ^{15}N, ^{13}C labeled km23 in NMR buffer containing 10 mg ml^{-1} Pf1 phage (Asla Biotech, Riga, Latvia) and by recording the appropriate NMR experiment. One-bond ^{1}H–^{15}N RDCs ($^{1}D_{NH}$) were measured by recording a 2-D IPAP-HSQC[65] with ^{15}N labeled protein. One-bond ^{15}N–$^{13}C'$ ($^{1}D_{NC'}$), one-bond $^{13}C^{\alpha}$–$^{13}C'$ ($^{1}D_{C\alpha C'}$), one-bond $^{1}H^{\alpha}$–$^{13}C^{\alpha}$ ($^{1}D_{H\alpha C\alpha}$), and two-bond $^{13}C'$–^{1}H ($^{2}D_{C'H}$) RDCs were measured with ^{13}C, ^{15}N labeled protein by recording a 2-D ^{1}H–^{15}N HSQC with $^{13}C'$ coupling in the indirect dimension, a $^{13}C^{\alpha}$-coupled 3-D HNCO,[66] a 3-D (HA)CA(CO)NH,[67] and a $^{13}C'$-coupled 2-D ^{1}H–^{15}N HSQC, respectively. Backbone ϕ and ψ restraints were obtained by analysis of the assigned chemical shifts using the program TALOS,[39] and in the case of ϕ, by additionally measuring $^{3}J_{HN\alpha}$ couplings using an HNHA experiment.[68]

Structure calculations

NOE restraints were grouped into three distance ranges, 1.8–2.7 Å (1.8–2.9 Å for distances involving ^{15}N-bound protons), 1.8–3.3 Å (1.8–3.5 Å for distances involving ^{15}N-bound protons), and 1.8–5.0 Å. Upper distances for restraints involving methyl protons were increased by 0.5 Å. Distances involving methyl protons, aromatic ring protons, and non-stereospecifically assigned methylene protons were represented as r^{-6} sum, $\sqrt[-1/6]{(\sum_{ij} r_{ij}^{-6})}$. Structures were determined from a total of 1660 experimental restraints, including 1121 distance restraints, 70 chemical shift derived ϕ and ψ restraints, 66 $^{3}J_{HN\alpha}$ restraints, and 333 RDC restraints (Table 1). Symmetry of the dimer was enforced by additionally including non-crystallographic restraints for backbone N, C^{α}, and C' atoms. Structures were calculated by using distance geometry and simulated annealing protocols[69] in torsion angle space[70] with the program X-PLOR-NIH.[38] Agreement of the calculated NMR structures with the experimentally measured RDC data was calculated using the program PALES.[41]

Backbone ^{15}N relaxation parameters

Backbone amide ^{15}N T_1, ^{15}N T_2, and ^{15}N–{^{1}H} NOE relaxation data sets were recorded in an interleaved manner at 42 °C at magnetic field strengths of 14.1 and 16.4 T (corresponding to ^{15}N frequencies of 60.81 MHz and 70.95 MHz, respectively) using ^{1}H-detected pulse schemes as described.[71] The T_1 and T_2 data sets were each collected using a total of 32 scans (eight scans per cycle, four cycles), an ^{15}N acquisition time of 136 ms, and a recycle time of 1.0 s. The T_1 and T_2 data sets were acquired using 12 delay times, which varied between 16–3600 ms and 16–400 ms, respectively. The spacing between the center of the ^{15}N π refocusing pulses (80 μs) in the CPMG of the ^{15}N T_2 experiment was 1 ms. The NOE data were recorded using 128 scans per point with a total ^{15}N acquisition time of 136 ms. The T_1 and T_2 relaxation times were obtained by fitting relative peak heights as a function of T_1 or T_2 delay time to a two parameter exponential. The errors in individual T_1 and T_2 measurements were estimated by Monte Carlo simulations.[72] NOE values were obtained by taking the ratio of peak intensities from experiments performed with and without ^{1}H presaturation and by applying a correction to take into account the incomplete recovery of both ^{15}N and ^{1}H magnetization.[73]

Modeling of the rotational diffusion tensor

The rotational diffusional anisotropy of km23 was modeled assuming axial symmetry. The relaxation data used for the calculation consisted of experimental T_1/T_2 ratios for 68 residues. Excluded from these calculations were 15 residues identified using the criteria described by Barbato[74] as undergoing exchange or high amplitude internal motion on the ns-ps time-scale. Amide bond vector orientations were calculated from the ten lowest energy NMR structures. The parameters describing the diffusion tensor, τ_{avg}, $D_{\|}/D_{\perp}$, θ, ϕ, were obtained by minimizing the quantity χ^2:

$$\chi^2 = \frac{1}{n}\sum_{1}^{n}[(T_1^{exp}/T_2^{exp}) - (T_1^{calc}/T_2^{calc})]/(T_1^{err}/T_2^{err}) \quad (1)$$

using the computational strategy described by Tjandra.[45] The statistical significance of the fit was assessed by repeating the fitting procedure after having randomized the residue numbers in the T_1/T_2 data table.

The km23 diffusion tensor was modeled by calculating the components of the inertia tensor from the coordinates of the km23 NMR structures. The axial ratio of the diffusion tensor was then approximated using the relation:

$$D_{\|}/D_{\perp} = [0.75(2(I_{\perp}/I_{\|}) - 1)]^{1/2} \quad (2)$$

This equation applies to a perfect ellipsoid[75] and therefore only roughly approximates the extent of diffusional anisotropy based upon the inertia calculation.

Modeling of internal motion

The internal dynamics of km23 were assessed by analyzing the experimental ^{15}N relaxation parameters using the model-free formalism[76,77] and by assuming that the protein tumbles as an axially symmetric rotor. This was accomplished using the program ModelFree4 and the model selection strategy based on F-statistics described by Mandel.[47] Five different models for internal motion were considered, S^2 (model 1), S^2, τ_e (model 2), S^2, R_{ex} (model 3), S^2,τ_e,R_{ex} (model 4), and S^2, S_f^2, τ_e (model 5).

Atomic coordinates accession codes

The km23 chemical shift assignments have been

deposited in the BMRB database under accession code 6527. The ensemble of low energy structures has been deposited in the RCSB database under accession code 1Z09.

Acknowledgements

Dr Virgil Schirff is thanked for collecting the analytical ultracentrifugation data. This work was supported by NCI grant CA100239, including an NMR Supplement awarded as CA100239-S1, to K.M.M. Additional financial support was provided by the Robert A. Welch Foundation (AQ1431 to A.P.H.), the Dept of Defense (DAMD17-03-0287 to K.M.M.), the NIH (GM58670 and RR13879 to A.P.H., CA92889 and CA90765 to K.M.M., and CA54174 to the Macromolecular Structure Shared Resource of the San Antonio Cancer Institute), the NSF (DBI-9974819 to B.D.) and the San Antonio Life Science Institute (10001642 to B.D.).

Supplementary Data

Supplementary data associated with this article can be found, in the online version, at doi:10.1016/j.jmb.2005.07.002

References

1. Vallee, R. B., Williams, J. C., Varma, D. & Barnhart, L. E. (2004). Dynein: an ancient motor protein involved in multiple modes of transport. *J. Neurobiol.* **58**, 189–200.
2. Gunawardena, S. & Goldstein, L. S. (2004). Cargo-carrying motor vehicles on the neuronal highway: transport pathways and neurodegenerative disease. *J. Neurobiol.* **58**, 258–271.
3. King, S. M. (2000). The dynein microtubule motor. *Biochim. Biophys. Acta*, **1496**, 60–75.
4. Vale, R. D. (2003). The molecular motor toolbox for intracellular transport. *Cell*, **112**, 467–480.
5. Vallee, R. B. & Sheetz, M. P. (1996). Targeting of motor proteins. *Science*, **271**, 1539–1544.
6. Harada, A., Takei, Y., Kanai, Y., Tanaka, Y., Nonaka, S. & Hirokawa, N. (1998). Golgi vesiculation and lysosome dispersion in cells lacking cytoplasmic dynein. *J. Cell Biol.* **141**, 51–59.
7. Vallee, R. B. & Hook, P. (2003). Molecular motors: a magnificent machine. *Nature*, **421**, 701–702.
8. Sakato, M. & King, S. M. (2004). Design and regulation of the AAA microtubule motor dynein. *J. Struct. Biol.* **146**, 58–71.
9. Bowman, A. B., Patel-King, R. S., Benashski, S. E., McCaffery, J. M., Goldstein, L. S. & King, S. M. (1999). Drosophila roadblock and Chlamydomonas LC7: a conserved family of dynein-associated proteins involved in axonal transport, flagellar motility, and mitosis. *J. Cell Biol.* **146**, 165–180.
10. Tang, Q., Staub, C. M., Gao, G., Jin, Q., Wang, Z., Ding, W. *et al*. (2002). A novel transforming growth factor-β receptor-interacting protein that is also a light chain of the motor protein dynein. *Mol. Biol. Cell*, **13**, 4484–4496.
11. Susalka, S. J., Nikulina, K., Salata, M. W., Vaughan, P. S., King, S. M., Vaughan, K. T. & Pfister, K. K. (2002). The roadblock light chain binds a novel region of the cytoplasmic Dynein intermediate chain. *J. Biol. Chem.* **277**, 32939–32946.
12. Jaffrey, S. R. & Snyder, S. H. (1996). PIN: an associated protein inhibitor of neuronal nitric oxide synthase. *Science*, **274**, 774–777.
13. Fan, J. S., Zhang, Q., Li, M., Tochio, H., Yamazaki, T., Shimizu, M. & Zhang, M. (1998). Protein inhibitor of neuronal nitric-oxide synthase, PIN, binds to a 17-amino acid residue fragment of the enzyme. *J. Biol. Chem.* **273**, 33472–33481.
14. Puthalakath, H., Huang, D. C., O'Reilly, L. A., King, S. M. & Strasser, A. (1999). The proapoptotic activity of the Bcl-2 family member Bim is regulated by interaction with the dynein motor complex. *Mol. Cell.* **3**, 287–296.
15. Puthalakath, H., Villunger, A., O'Reilly, L. A., Beaumont, J. G., Coultas, L., Cheney, R. E. *et al*. (2001). Bmf: a proapoptotic BH3-only protein regulated by interaction with the myosin V actin motor complex, activated by anoikis. *Science*, **293**, 1829–1832.
16. Schnorrer, F., Bohmann, K. & Nusslein-Volhard, C. (2000). The molecular motor dynein is involved in targeting swallow and bicoid RNA to the anterior pole of Drosophila oocytes. *Nature Cell Biol.* **2**, 185–190.
17. Raux, H., Flamand, A. & Blondel, D. (2000). Interaction of the rabies virus P protein with the LC8 dynein light chain. *J. Virol.* **74**, 10212–10216.
18. Vadlamudi, R. K., Bagheri-Yarmand, R., Yang, Z., Balasenthil, S., Nguyen, D., Sahin, A. A. *et al*. (2004). Dynein light chain 1, a p21-activated kinase 1-interacting substrate, promotes cancerous phenotypes. *Cancer Cell*, **5**, 575–585.
19. Nagano, F., Orita, S., Sasaki, T., Naito, A., Sakaguchi, G., Maeda, M. *et al*. (1998). Interaction of Doc2 with Tctex-1, a light chain of cytoplasmic dynein. Implication in dynein-dependent vesicle transport. *J. Biol. Chem.* **273**, 30065–30068.
20. Campbell, K. S., Cooper, S., Dessing, M., Yates, S. & Buder, A. (1998). Interaction of p59fyn kinase with the dynein light chain, Tctex-1, and colocalization during cytokinesis. *J. Immunol.* **161**, 1728–1737.
21. Tai, A. W., Chuang, J. Z., Bode, C., Wolfrum, U. & Sung, C. H. (1999). Rhodopsin's carboxy-terminal cytoplasmic tail acts as a membrane receptor for cytoplasmic dynein by binding to the dynein light chain Tctex-1. *Cell*, **97**, 877–887.
22. Fan, J., Zhang, Q., Tochio, H., Li, M. & Zhang, M. (2001). Structural basis of diverse sequence-dependent target recognition by the 8 kDa dynein light chain. *J. Mol. Biol.* **306**, 97–108.
23. Wang, W., Lo, K. W., Kan, H. M., Fan, J. S. & Zhang, M. (2003). Structure of the monomeric 8-kDa dynein light chain and mechanism of the domain-swapped dimer assembly. *J. Biol. Chem.* **278**, 41491–41499.
24. Liang, J., Jaffrey, S. R., Guo, W., Snyder, S. H. & Clardy, J. (1999). Structure of the PIN/LC8 dimer with a bound peptide. *Nature Struct. Biol.* **6**, 735–740.
25. Williams, J. C., Xie, H. & Hendrickson, W. A. (2005). Crystal structure of dynein light chain TCTEX-1. *J. Biol. Chem.* **23**, 21981–21986.
26. Wu, H., Maciejewski, M. W., Takebe, S. & King, S. M.

(2005). Solution structure of the Tctex1 dimer reveals a mechanism for dynein-cargo interactions. *Structure*, **13**, 213–223.
27. Fan, J. S., Zhang, Q., Tochio, H. & Zhang, M. (2002). Backbone dynamics of the 8 kDa dynein light chain dimer reveals molecular basis of the protein's functional diversity. *J. Biomol. NMR*, **23**, 103–114.
28. Jin, Q., Ding, W., Staub, C. M., Gao, G., Tang, Q. & Mulder, K. M. (2005). Requirement of km23 for TGFβ-mediated growth inhibition and induction of fibronectin expression. *Cell. Signal*. In the Press (available online March 31, 2005).
29. Massagué, J., Blain, S. W. & Lo, R. S. (2000). TGFβ signaling in growth control, cancer, and heritable disorders. *Cell*, **103**, 295–309.
30. Yue, J. & Mulder, K. M. (2001). Transforming growth factor-β signal transduction in epithelial cells. *Pharmacol. Ther.* **91**, 1–34.
31. Ding, W., Tang, Q., Espina, V., Liotta, L. A., Mauger, D. T. & Mulder, K. M. (2005). A TGF-β receptor-interacting protein frequently mutated in epithelial ovarian cancer. *Cancer Res.*. Aug 1, In the Press.
32. Koonin, E. V. & Aravind, L. (2000). Dynein light chains of the Roadblock/LC7 group belong to an ancient protein superfamily implicated in NTPase regulation. *Curr. Biol.* **10**, R774–R776.
33. Lunin, V. V., Munger, C., Wagner, J., Ye, Z., Cygler, M. & Sacher, M. (2004). The structure of the MAPK scaffold, MP1, bound to its partner, p14. A complex with a critical role in endosomal map kinase signaling. *J. Biol. Chem.* **279**, 23422–23430.
34. Kurzbauer, R., Teis, D., de Araujo, M. E., Maurer-Stroh, S., Eisenhaber, F., Bourenkov, G. P. *et al*. (2004). Crystal structure of the p14/MP1 scaffolding complex: how a twin couple attaches mitogen-activated protein kinase signaling to late endosomes. *Proc. Natl Acad. Sci. USA*, **101**, 10984–10989.
35. Schuck, P. (2000). Size-distribution analysis of macromolecules by sedimentation velocity ultracentrifugation and Lamm equation modeling. *Biophys. J.* **78**, 1606–1619.
36. Demeler, B. & Saber, H. (1998). Determination of molecular parameters by fitting sedimentation data to finite-element solutions of the Lamm equation. *Biophys. J.* **74**, 444–454.
37. Wishart, D. S. & Sykes, B. D. (1994). The ^{13}C chemical-shift index: a simple method for the identification of protein secondary structure using ^{13}C chemical shift data. *J. Biomol. NMR*, **4**, 171–180.
38. Schwieters, C. D., Kuszewski, J. J., Tjandra, N. & Clore, G. M. (2003). The Xplor-NIH NMR molecular structure determination package. *J. Magn. Reson.* **160**, 65–73.
39. Cornilescu, G., Delaglio, F. & Bax, A. (1999). Protein backbone angle restraints from searching a database for chemical shift and sequence homology. *J. Biomol. NMR*, **13**, 289–302.
40. Hansen, M. R., Mueller, L. & Pardi, A. (1998). Tunable alignment of macromolecules by filamentous phage yields dipolar coupling interactions. *Nature Struct. Biol.* **5**, 1065–1074.
41. Zweckstetter, M. & Bax, A. (2000). Prediction of sterically induced alignment in a dilute liquid crystalline phase: aid to protein structure determination by NMR. *J. Am. Chem. Soc.* **122**, 3791–3792.
42. Bax, A., Kontaxis, G. & Tjandra, N. (2001). Dipolar couplings in macromolecular structure determination. *Methods Enzymol.* **339**, 127–174.
43. Laskowski, R. A., MacArthur, M. W., Moss, D. S. & Thornton, J. M. (1993). PROCHECK: a program to check the stereochemical quality of protein structures. *J. Appl. Crystallog.* **26**, 283–291.
44. Osborne, M. J. & Wright, P. E. (2001). Anisotropic rotational diffusion in model-free analysis for a ternary DHFR complex. *J. Biomol. NMR*, **19**, 209–230.
45. Tjandra, N., Feller, S. E., Pastor, R. W. & Bax, A. (1995). Rotational diffusion anisotropy of human ubiquitin from ^{15}N NMR relaxation. *J. Am. Chem. Soc.* **117**, 12562–12566.
46. Tjandra, N., Wingfield, P., Stahl, S. & Bax, A. (1996). Anisotropic rotational diffusion of perdeuterated HIV protease from ^{15}N NMR relaxation measurements at two magnetic fields. *J. Biomol. NMR*, **8**, 273–284.
47. Mandel, A. M., Akke, M. & Palmer, A. G., III (1995). Backbone dynamics of *Escherichia coli* ribonuclease HI: correlations with structure and function in an active enzyme. *J. Mol. Biol.* **246**, 144–163.
48. Ding, W. & Mulder, K. M. (2004). km23: a novel TGFβ signaling target altered in ovarian cancer. In *Molecular Targeting and Signal Transduction (Cancer Treatment and Research)* (Kumar, R., ed.), vol. 119, pp. 315–327, Kluwer Academic Publishers, Boston/New York/Dordrecht/London.
49. Livingstone, C. D. & Barton, G. J. (1993). Protein sequence alignments: a strategy for the hierarchical analysis of residue conservation. *Comput. Appl. Biosci.* **9**, 745–756.
50. Jiang, J., Yu, L., Huang, X., Chen, X., Li, D., Zhang, Y. *et al*. (2001). Identification of two novel human dynein light chain genes, DNLC2A and DNLC2B, and their expression changes in hepatocellular carcinoma tissues from 68 Chinese patients. *Gene*, **281**, 103–113.
51. Demeler, B. (2005). UltraScan Software, University of Texas Health Science Center at San Antonio, Department of Biochemistry. http://ultrascan.uthscsa.edu
52. Laue, T. M., Shah, B. D., Ridgeway, T. M. & Pelletier, S. L. (1992). Analytical Ultracentrifugation in Biochemistry and Polymer Science. In *Proteins Amino Acids and Peptides as Ions and Dipolar Ions* (Harding, S. E., Rowe, A. J. & Horton, J. C., eds), pp. 90–125, Royal Society of Chemistry, Cambridge.
53. Cohn, E. J. & Edsall, J. T. (1943). *Proteins Amino Acids and Peptides as Ions and Dipolar Ions*, Reinhold, New York pp. 157.
54. Neri, D., Szyperski, T., Otting, G., Senn, H. & Wuthrich, K. (1989). Stereospecific nuclear magnetic resonance assignments of the methyl groups of valine and leucine in the DNA-binding domain of the 434 repressor by biosynthetically directed fractional ^{13}C labeling. *Biochemistry*, **28**, 7510–7516.
55. Delaglio, F., Grzesiek, S., Vuister, G. W., Zhu, G., Pfeifer, J. & Bax, A. (1995). NMRPIPE—a multi-dimensional spectral processing system based on Unix Pipes. *J. Biomol. NMR*, **6**, 277–293.
56. Johnson, B. A. & Blevins, R. A. (1994). NMRView—a computer-program for the visualization and analysis of NMR data. *J. Biomol. NMR*, **4**, 603–614.
57. Yamazaki, T., Lee, W., Revington, M., Mattiello, D. L., Dahlquist, F. W., Arrowsmith, C. H. & Kay, L. E. (1994). An HNCA pulse scheme for the backbone assignment of N-15,C-13,H-2-labeled proteins—application to a 37-kDa Trp repressor DNA complex. *J. Am. Chem. Soc.* **116**, 6464–6465.
58. Wittekind, M. & Mueller, L. (1993). HNCACB, a high-sensitivity 3-D NMR experiment to correlate amide-proton and nitrogen resonances with the alpha-carbon and beta-carbon resonances in proteins. *J. Magn. Reson. ser. B*, **101**, 201–205.

59. Grzesiek, S. & Bax, A. (1993). Amino acid type determination in the sequential assignment procedure of uniformLy $^{13}C/^{15}N$-enriched proteins. *J. Biomol. NMR*, **3**, 185–204.
60. Kay, L. E., Ikura, M., Tschudin, R. & Bax, A. (1990). 3-Dimensional triple-resonance NMR-spectroscopy of isotopically enriched proteins. *J. Magn. Reson.* **89**, 496–514.
61. Grzesiek, S., Anglister, J. & Bax, A. (1993). Correlation of backbone amide and aliphatic side-chain resonances in C-13/N-15-enriched proteins by isotropic mixing of C-13 magnetization. *J. Magn. Reson. ser. B*, **101**, 114–119.
62. Kay, L. E., Xu, G. Y., Singer, A. U., Muhandiram, D. R. & Formankay, J. D. (1993). A gradient-enhanced HCCH-TOCSY experiment for recording side-chain H-1 and C-13 correlations in H_2O samples of proteins. *J. Magn. Reson. ser. B*, **101**, 333–337.
63. Zwahlen, C., Legault, P., Vincent, S. J. F., Greenblatt, J., Konrat, R. & Kay, L. E. (1997). Methods for measurement of intermolecular NOEs by multinuclear NMR spectroscopy: application to a bacteriophage lambda N-peptide/boxB RNA complex. *J. Am. Chem. Soc.* **119**, 6711–6721.
64. Muhandiram, D. R., Farrow, N. A., Xu, G. Y., Smallcombe, S. H. & Kay, L. E. (1993). A gradient C-13 NOESY-HSQC experiment for recording NOESY spectra of C-13 labeled proteins dissolved in H_2O. *J. Magn. Reson. ser. B*, **102**, 317–321.
65. Ottiger, M., Delaglio, F. & Bax, A. (1998). Measurement of J and dipolar couplings from simplified two-dimensional NMR spectra. *J. Magn. Reson.* **131**, 373–378.
66. Grzesiek, S. & Bax, A. (1992). Improved 3D triple-resonance NMR techniques applied to a 31-kDa protein. *J. Magn. Reson.* **96**, 432–440.
67. Tjandra, N. & Bax, A. (1997). Large variation in $^{13}C^{\alpha}$ chemical shift anisotropy in proteins correlate with secondary structure. *J. Am. Chem. Soc.* **119**, 9576–9577.
68. Vuister, G. W. & Bax, A. (1994). Measurement of four-bond HN-H alpha *J*-couplings in staphylococcal nuclease. *J. Biomol. NMR*, **4**, 193–200.
69. Nilges, M., Clore, G. M. & Gronenborn, A. M. (1988). Determination of three-dimensional structures of proteins from interproton distance data by hybrid distance geometry-dynamical simulated annealing calculations. *FEBS Letters*, **229**, 317–324.
70. Schwieters, C. D. & Clore, G. M. (2001). Internal coordinates for molecular dynamics and minimization in structure determination and refinement. *J. Magn. Reson.* **152**, 288–302.
71. Kay, L. E., Nicholson, L. K., Delaglio, F., Bax, A. & Torchia, D. A. (1992). Pulse sequences for removal of the effects of cross-correlation between dipolar and chemical-shift anisotropy relaxation mechanism on the measurement of heteronuclear T_1 and T_2 values in proteins. *J. Magn. Reson.* **97**, 359–375.
72. Press, W. H., Flannery, B. P., Teukolsky, S. A. & Vetterling, W. T. (1988). *Numerical Recipes in C*, Cambridge University Press, Cambridge, UK.
73. Freedberg, D. I., Ishima, R., Jacob, J., Wang, Y. X., Kustanovich, I., Louis, J. M. & Torchia, D. A. (2002). Rapid structural fluctuations of the free HIV protease flaps in solution: relationship to crystal structures and comparison with predictions of dynamics calculations. *Protein Sci.* **11**, 221–232.
74. Barbato, G., Ikura, M., Kay, L. E., Pastor, R. W. & Bax, A. (1992). Backbone dynamics of calmodulin studied by ^{15}N relaxation using inverse detected two-dimensional NMR spectroscopy: the central helix is flexible. *Biochemistry*, **31**, 5269–5278.
75. Copie, V., Tomita, Y., Akiyama, S. K., Aota, S., Yamada, K. M., Venable, R. M. *et al*. (1998). Solution structure and dynamics of linked cell attachment modules of mouse fibronectin containing the RGD and synergy regions: comparison with the human fibronectin crystal structure. *J. Mol. Biol.* **277**, 663–682.
76. Lipari, G. & Szabo, A. (1982). Model-free approach to the interpretation of nuclear magnetic resonance relaxation in macromolecules. 2. Analysis of experimental results. *J. Am. Chem. Soc.* **104**, 4559–4570.
77. Clore, G. M., Szabo, A., Bax, A., Kay, L. E., Driscoll, P. C. & Gronenborn, A. M. (1990). Deviations from the simple 2-parameter model-free approach to the interpretation of N-15 nuclear magnetic-relaxation of proteins. *J. Am. Chem. Soc.* **112**, 4989–4991.
78. Woessner, D. E. (1962). Nuclear spin relaxation in ellipsoids undergoing rotational brownian motion. *J. Chem. Phys.* **37**, 647–654.

Edited by M. F. Summers

(Received 21 April 2005; received in revised form 5 July 2005; accepted 5 July 2005)
Available online 20 July 2005